Machine Learning-Based Reconstruction of Neuronal Networks from Calcium Imaging Signals

Derek Low

A Senior Project Submitted to

The Division of Science, Mathematics, and Computing

of Bard College

Annandale-On-Hudson, New York

2017-2018

Dedications and Acknowledgements

I'll work on this part last

-Kerri-Ann

-Arseny Khakhalin

-Maia, Sadie, Patrycja

- Swim Team, Swimming Coaches

-Kevin, Liam, Kabir, Halina, Emma, Mary, Ben

- Eli, Taysa

- Lily, Kara

- Parents

- Myself

Contents

List of Figures

0.1 Brief Description

~~Activity of neuronal networks can be recorded via Calcium Imaging.~~ In this study, we develop a machine learning approach to reconstructing network connectivity from calcium imaging data.

0.2 Abstract

One of the major areas of research in computational neuroscience is focused on relating the connections within populations of neurons to the signaling activity of these populations. Methods of reconstructing structural neuronal network connectivity are limited and, in large populations, technically infeasible. Current methods that reconstruct networks of large populations relate connectivity to calcium imaging recordings of these networks. Here, we introduce a machine-learning approach to inferring connectivity from spike-time data extracted from calcium imaging recordings. First, we simulate populations of neurons with the NEST simulator to produce downsampled spike-trains. We develop a model based on neural networks, which is a widely applied machine-learning method. The model is updated with gradient descent on the error via backpropagation, and the performance is compared to the widely used cross-correlation method of extracting functional connectivity. We then train the models on simulated data and *in-vivo* calcium imaging data from *Xenopus Laevis* tadpoles.

1 Introduction

1.1 The Neuron

Neurons are fundamental to human cognition, and encode for a large range of activities such as movement, speech, and decision making. The interactions between neurons throughout the human body have been studied at microscopic levels, with focus on the specific mechanisms and dynamics of neurons that allow for propagation of signals from one neuron to the next neuron (Bean, 2007). Networks of neurons have also been studied at macroscopic levels, relating specific regions to distinct functions, such as the relationship between the brain and human capabilities of cognitive control and activity, or the specific activity of particular regions of the brain (Biswal et al., 1995; Mazzoni et al., 2007). However, the precise connectivity patterns of neurons, and the relationship between this organization and its possible functions, are not fully understood (Bock et al., 2011). Analysis of the patterns of connections in populations of neurons indicate that these networks can be characterized by network properties. Therefore, understanding these connections may provide insight to the function and activity of these populations of neurons, and may imply a relationship between functional and structural connectivity.

The transmission of signals within parts of neurons is partially mediated by the electrical potential difference between a neuron and its surrounding environment, known as the membrane potential. The earliest and most influential studies concerning the effects of ions in neurons were conducted by Hodgkin, Huxley, and Katz nearly 70 years ago, and clearly indicated the relationship between ion concentration and the activity of neurons. Giant squid axons in lower sodium environments maintained a lower resting potential, as well as a weaker and delayed action potential (Hodgkin and Katz, 1949). Changes in concentrations of ions, distributed in varying concentrations throughout the nervous system, mediate neuron activity by changing this membrane potential. In a state of low activity, this membrane defaults to a polarized state of negative electrical potential, referred to as the resting membrane potential (Purves et al. pp.31, 2004,). When the membrane potential moves in the positive direction, signal propagation along the neuron occurs.

Communication between neurons occur at the synapse, a structure of connection between two neurons. The communication occurs via a synaptic potential, a signal from the pre-synaptic to the post-synaptic neuron, and is initiated by the release of neurotransmitters from the presynap-

tic neuron that interact with receptors in the postsynaptic neuron. Synaptic potentials are either excitatory, increasing the membrane potential of the neuron towards positive values (depolarization), or inhibitory, reducing potential towards negative values (hyperpolarization) (Bean, 2007). The resulting depolarization due to the excitatory post-synaptic potentials (EPSPs) increases the membrane potential towards higher positive values, until a specific threshold is reached (Bean, 2007). Once a specific depolarization threshold is reached, an action potential is generated, and propagates along the neuron until it reaches another synapse, at which point the cycle of neurotransmitter release, synaptic potential, and action potential propagation cycle may be repeated (Bean, 2007).

The propagation of action potentials involves constant changes to the electrochemical gradients of the neurons by the opening and closing of ion channels in the membrane. The ion channels involved in generating action potentials, mediating and raising membrane potentials towards distinct states of polarization during neuronal signaling include the voltage-gated ion channels, specifically the sodium (Na^+), potassium (K^+) and calcium (Ca^{2+}) channels. However, while these channels serve similar purposes of allowing passage of certain ions and restricting passage of other ions, the time of activation of each type of channel demonstrated their distinct impacts on propagation. The depolarization of the neuron, and consequent upswing in membrane potential towards positive values, is caused by the influx of sodium from the extracellular medium into the cell; this influx is caused by the opening of sodium channels following an EPSP, prior to the membrane potential reaching the threshold potential and the initiation of an action potential. (Hodgkin and Katz, 1949; Hodgkin and Huxley, 1952). The resulting repolarization and hyperpolarization stages preceding the return to resting membrane potential result from the efflux of potassium; this efflux is a delayed response to the initiation of the action potential, indicating a delayed opening of potassium channels following the opening of sodium channels (Hodgkin and Huxley, 1952). This signal propagation is referred to as a neuronal *spike*, and is the primary method of observing neuronal activity in neuroscience research.

1.2   Network Neuroscience

The structure of populations of neurons has an effect on the activity of these neurons. Therefore, understanding the organization of neurons is major topic in neuroscientific research. One primary

area of focus in studying these networks is the mammalian cerebral cortex. The mammalian cerebral cortex contains the most recently evolved areas of the human brain. In particular, the human cerebral cortex is regarded as the most complex part of the brain, responsible for various mammalian and human-specific cognitive abilities (Rakic, 2006). The cerebral cortex is a region of the brain comprised of several subregions: the motor, sensory, and associative areas. The majority of the cortex is referred to as the neocortex, explicitly defined as the layers of the cortex comprised of six cellular layers (Purves et al, 2012). Research focused in the neocortex refer to cortical circuits, a general term for larger neuronal networks located in the cortex and cortical ensembles, referring to coactive networks of neurons that possibly comprise cortical circuits (Carrillo-Reid et al., 2016; Hamm et al., 2017,; Bock et al., 2011). Due to the involvement of the neocortex in a variety of functions, such as movement, sensation, and cognition, the cerebral cortex is a significant target for study.

The study of connectivity in the brain has a wide range of application. For example, some studies concerning the cerebral cortex focus on disease and the derivative cortical ensembles that are representative of the disease. One such example is schizophrenia, a disorder characterized by hallucinations, delusions, disordered thoughts, and loss of emotional expression (Purves et al., 2012). As a neurological disorder accompanied with altered neuromodulation, excitatory and inhibitory neuron balance, and development, as well as altered connectivity at a higher scale, schizophrenia is a target of research concerned with the effects of these neurological changes on the presentation and characterization of the disorder. A study conducted by Hamm et al., observed cortical ensembles in mice models that displayed symptoms of schizophrenia via administration of ketamine or were genetically dispositioned towards development of schizophrenia. Imaging of awake mice models allowed for analysis of activity in cortical ensembles, and the relationships and recurrent patterns in sub-ensembles (local neuronal networks). The results of the study indicated several alterations to cortical activity of the symptomatic mice, such as impact of altered dynamics of local networks on cortical ensembles, and the necessity of long-term changes to cortical connectivity to initiate changes in cortical ensemble reliability in propagation of patterns of activity consistent with schizophrenia (Hamm et al., 2017). These models allow us to understand that neuronal connectivity patterns, upon change, alter the resulting activity patterns, and altered activity patterns have impacts on these connectivities.

The relationship between functionality and connectivity has been demonstrated in ~~further~~ additional contexts, such as in motor neurons of human patients by relating the movement of fingers on each hand to the fluctuations in signal intensity of the sensorimotor cortex during echo-planar functional magnetic resonance imaging (fMRI)(Biswal et al., 1995). Additionally, between two related, yet distinct, activities, the functional connectivity of neurons can overlap; such is the case in the instance of motor imagery, or the mental performance of certain motor acts not accompanied by physical performance of these acts, and the accompanying physical performance of the same motor acts (Porro et al., 1996). The hippocampus of the human brain demonstrates a similar relationship of functional connectivity with particular activities; young adults display higher levels of activity in the ventral prefrontal and extrastriate regions of the cortex correlated with higher levels of hippocampus activity during encoding of words and pictures of objects. In contrast, older adults display higher levels of activity in the dorsolateral prefrontal and parietal regions of the cortex with comparable levels of activity in the hippocampus to younger adults during similar trials (Grady et al., 2003). The higher activity in particular regions implies different manners by which adults of differing ages process information concerning similar tasks, where hippocampus and brain activity are related to better recognition in younger adults, and improved memory performance in older adults. These findings indicate a shift in explicit connectivity between portions of the brain, and changes to functional connectivity related to human aging (Grady et al., 2003).

1.2.1 Network Metrics

Network science provides a framework through which populations of neurons may be analyzed for their structural and functional connectivities by expanding and formalizing the terminologies and definitions for the purposes of neuronal network analysis. For example, cliques, or all-to-all connected networks, of neuronal populations have been studied as a method of relating structural to functional connectivities of neuronal populations. ~~In the context of neuronal networks, cliques are further studied as directed cliques.~~ Where standard cliques are bidirectional, allowing a single connection for both information transfer from a source neuron to a target neuron and information transfer in the inverse direction, directed cliques do not allow for bidirectional information transfer. (Reimann et al., 2017). For a given connection in a directed clique from a source neuron to a target neuron, there is no direct connection from the target neuron to the source neuron, though there may

be an intermediary neuron allowing for a connection in the inverse direction. The reconstruction and viewing of networks as compositions of cliques suggests that, in neocortical microcircuits, information is processed by the formation and disintegration of these cliques, depending on the nature of the stimulus (Reimann et al., 2017).

Analysis of these patterns of connectivity, or the microcircuitry, of neurons in regions of the brain indicate the possibility of the scale-free nature of microcircuits. A scale-free network is defined as a network with the degree distribution following a power-law (Massobrio et al., 2015, Tetzlaff et al., 2010). The degree distribution of a network is defined as the probabilities of a node having a particular degree within a network; degree distributions are often displayed relating a specific degree to the rate of occurrence, or the probability (Hernandez and Meighem, 2011; Massobrio et al., 2015, Tetzlaff et al., 2010). The degree distribution of a network is often referred to as a metric of resilience (Rubinov and Sporns, 2010; Hernandez and Meighem, 2011). A network following a power-law distribution indicates a network in which a majority of nodes contain a low number of connections, and a minority containing a high number of connections (Sporns et al., 2004, Tetzlaff et al., 2010, Massobrio et al., 2015). Therefore, these networks are fairly resilient to random removals of nodes, since the removal is likely to occur to nodes with low connections, resulting in low overall impact on the network. However, the removal of a node with a high number of connection could be critical to the function of the network (Rubinov and Sporns, 2010; Hernandez and Meighem, 2011;)

1.3   Calcium Imaging

A commonly employed method of recording activity of neurons is calcium imaging. ~~Neuron activity.~~ At every spiking event, these ions travel through the cell membrane of each neuron by movement through voltage-dependent ion channels, which are functionally altered by the voltage changes that occur in neurons.

The versatility and presence of calcium in neurons can be described by the large variety of neuronal processes related to it. Calcium performs several major roles in the function and management of biological cells; most notably, in the presynaptic neuron, an influx of calcium into the neuron triggers the release of neurotransmitter to the synapse via exocytosis (Katz and Miledi, 1967). Furthermore, presynaptically, residual calcium results in neural facilitation, a period in

which a successive depolarization of the presynaptic neuron, following the first depolarization event and release of neurotransmitter, raises the likelihood of neurotransmitter release (Katz and Miledi, 1967; Zucker, 1999). Postsynaptically, calcium is responsible for activating the synaptic plasticity cascade. These changes to the synapse, functionally initiated by interactions between calcium and the N-methyl-D-aspartate receptor (NMDA) and α-amino-3-hydroxy-5-methyl-4-isoxazolepropionic acid receptor (AMPA), result in changes to the sensitivity and, by extension, the interactions between the pre- and postsynaptic neurons (Zucker, 1999). The changes enhance or diminish the strength of the connection (potentiation and depression), in various temporal manners (short and long-term). For example, in the case of long-term potentiation (LTP), the influx of calcium into the postsynaptic neuron, and the resulting depolarization, result in the unblocking of the NMDA receptors, allowing for a further influx of calcium into the postsynaptic neuron and inducing LTP (Zucker 1999).Functions of calcium extend further than synaptic activity, and the ion is additionally responsible for biological functions such as cell apoptosis (Orrenius et al., 2003). Therefore, the abundance and utility of calcium, and the deeply integral relationship between calcium and neuron activity, suggest it to be a strong candidate for the purpose of imaging populations of neurons.

1.3.1   Calcium Indicators

As mentioned, calcium activity is dependent on the voltage changes of neurons and the responses of voltage-gated channels to voltage changes, and concentration is higher extracellularly until spike time. Therefore, introducing into the neurons an indicator that fluoresces when bound to calcium allows recording of calcium concentration and activity. Among the first discovered and applied calcium indicators is the protein aequorin (Shimomura et al., 1962), where the binding of the calcium to the three binding sites located on the protein results in photon emission (Grienberger and Konnerth, 2012). The necessity of the three calcium molecules, in combination with a controlled amount of indicator injected into these neurons, allows for a controlled fluorescence method that is directly related to the calcium concentration within the cell. However, the particular drawbacks of aequorin, such as a low protein stability and a relatively low fluorescence rate with regards to the amount of decomposition in the concentration of the protein, result in development of several superior and modern alternatives (Grienberger and Konnerth, 2012).

Modern calcium indicators are typically categorized as high-affinity or low-affinity, where high-

affinity indicates the most commonly used indicators with wide varieties of application. One such high-affinity calcium indicator is fura-2 (Grynkiewicz et al., 1985); this indicator operates by excitation with ultraviolet light, resulting in a fluorescence shift of the indicator; the fluorescence level changes when the molecule is bound to calcium, a property referred to as ratiometric, dual-wavelength, or dual-excitation (Grienberger and Konnerth, 2012). This particular indicator is applied to a variety of microscopy methods, including two-photon microscopy (discussed below), requiring slight modification by inclusion of green fluorescent protein (GFP) in the latter case (Grinberger and Konnerth, 2012).

1.3.2   Calcium Microscopy

The second component is the imaging, recording, and approximation of recorded data as a measurement of brain activity. There are several technologies employed in the recording of calcium indicator fluorescence; the technique used widely depends on the subject being recorded and quality of the imaging required. However, an equally wide range of techniques are available, and have particular benefits and drawbacks relating to the method and observed sample.

All microscopy techniques result in the photobleaching and phototoxicity of the observed specimens, resulting in photodamage (Svodoba et al., 2006). Another restricting factor in microscopy is photon scattering, a process in which a photon is absorbed by a molecule and re-emitted in a distinctly random direction, resulting in the blurring of the resulting microscopy image (Ntziachristos, 2010). Therefore, one aim relevant to employed microscopy techniques is the highest accumulation of imaging data with the lowest possible amount of photodamage to the observed specimen, and lowest photon scattering for image accuracy and clarity. Prior to the development of two photon microscopy in the 1990's (Denk et al., 1990), most microscopy methods used, such as confocal and wide-field fluorescence microscopy, suffered from the major drawback of having low tissue penetration depth due to photon scattering and, in the case of confocal microscopy, tissue degradation (Svodoba et al., 2006).

1.4   Xenopus Tadpoles

The *Xenopus Laevis* tadpole is an experimental model and has been used in a variety of studies, such as studies in developmental changes in responses to sensory stimuli, the role of neural activity

on changes in neural circuits, and the roles of excitatory and inhibitory connections on behavioral responses (Dong et al., 2008; Khakhalin et al., 2014; Ciarleglio et al., 2015). The inputs and outputs to tadpole neuronal networks in the optic tectum can be accessed *in vivo*, and calcium imaging data can be recorded from these networks (Xu et al., 2011; Khakhalin et al., 2014). For example, Xu et al., 2011 recorded large-scale neural activity via in-vivo calcium imaging to detect synchronous patterns of spiking across the population of neurons. In this study, spike trains of individual tectal neurons within a larger neuronal population were observed by recording the Ca^{2+} responses via a membrane-permeant Ca^{2+} indicator. The Ca^{2+} images recorded were first filtered and deconvolved, a method of reducing noise involving an algorithm to specifically reduce the imaging artifacts (Xu et al., 2011). In the case of calcium imaging, these artifacts primarily originate from the slow decays of calcium signals, and the slow decay nature restricts the imaging of spikes occurring in rapid succession. To counteract this effect, Xu et al., produced a deconvolution algorithm by selecting and loose-patch clamping a subset of tadpole tectal neurons to record the action potentials simultaneous with the calcium imaging (Xu et al., 2011). From this simultaneously recorded electrophysiological and calcium imaging data, a relationship between the more precise, smaller scale method (loose-patch clamp) and the less precise, larger scale method (calcium imaging) was developed for deconvolution of the calcium imaging signal. Analyzing the resulting deconvoluted data identified individual spike times from the signals produced by the calcium-sensitive dyes during visual stimulation (Xu et al., 2011).

1.5   Representing Networks of Neurons

The organization of neurons can be represented as a matrix, typically referred to as an adjacency or weight matrix. The matrix is an adjacency or weight matrix, depending on how these connections between neurons are represented, and what information is useful and preserved. Weight matrices assign values based on the strength of connections between neurons, and whether the source neuron is an excitatory or inhibitory neuron, while adjacency matrices are representative of whether or not there is a connection, and ignores the strength of these connections. For example, the following matrix describes connections between a population of three neurons:

	Neuron 1	Neuron 2	Neuron 3
Neuron 1	0	1	1
Neuron 2	0	0	0
Neuron 3	1	1	0
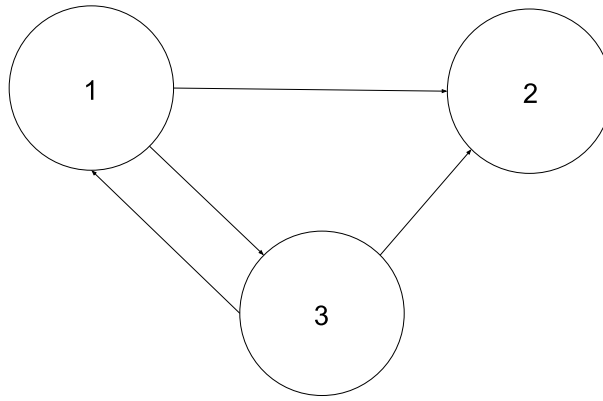
Figure 1: Sample Adjacency Matrix of Population Size 3. Diagonal indices represent self-connections. Labels along the columns represent the target, and labels along the rows represent the source e.g. the connection at Row 3, Column 2 (value of 1) is a connection from the pre-synaptic Neuron 3 to the post-synaptic Neuron 2. Note the lack of the inverse connection from Neuron 2 to Neuron 3 (value of 0).

Matrices such as the one above describe the connections between different neurons in an observed population, ~~with observed being an important keyword;~~ these neurons could have incoming connections from sources outside of the observed population, depending on the context of the observations. ~~One standard feature of~~ network matrices is the zero value along the diagonal, representative of a lack of a connection from a neuron to itself. In the example above, there is a directional connection between the outward axonal connection of Neuron 3 and the incoming dendritic connection of Neuron 1; therefore, assuming a positive value to represent an excitatory connection, spikes in Neuron 3 result in a voltage increase of Neuron 1. By this method of representation, the matrix can describe the relative strength and nature of all connections between neurons in the observed

population.

Currently, ~~our~~ methods of studying neurons and brain activity relies on techniques that observe activity at macroscopic (e.g. fMRI, PET, CAT, calcium imaging) or microscopic scales (e.g. electrodes and membrane potentials, patch clamp). However, there is no method of accurately imaging and representing larger networks of neurons in areas of the brain, or outgoing pathways from the brain. While machine learning algorithms may not provide exact mappings of networks, implementation of these algorithms is an opportunity to generate hypotheses concerning predicted connections and their relationships to the actual networks.

1.6 Current Approaches to Reconstruction

Several different frameworks of reconstruction have been offered to tackle the problem of inferring connectivity of neurons. While these reconstruction methods use different methods for evaluating activity and connectivity, they are typically applied to simulated neuron populations, where the ground truth of the activity is known, allowing evaluation on the accuracy of the model. Knowing the ground truth for comparison allows for the application of different metrics, such as Receiver Operating Character (ROC) curves, Area Under Curve (AUC), and network properties that are common between the predicted and ground truth networks (Garofalo et al., 2009).

1.6.1 Cross-Correlation

Cross-correlation is a widely applied similarity measurement method ~~across probability and statistics~~. In neuroscience, cross-correlation is applied as a comparison between the spiking time series of two neurons, measuring the frequency of spiking of one neuron relative to the frequency of spiking of another neuron (Garofalo et al., 2009). The frequency evaluates to a probability of a spike of neuron Y after some time shift τ (or $t + \tau$) relative to a spike of neuron X at time t. A histogram estimating the cross-correlation between two spike trains is the cross-correlogram of the two spike trains, ~~and a~~ correlogram estimates the autocorrelation of a spike train, ~~or~~ a correlation of a spike train with itself. The resulting cross-correlogram contains bins, where each bin contains the number of spikes that occur at that particular time lag across all reference spikes (Knox, 1981). Therefore, in a correlogram comparing a spike train to itself, the bin with the highest count contains a count equivalent to the number of spikes occurring in the spike train. Calculating the cross-correlogram

across all possible neuron connections in a population, and retaining the highest spikes found in a single bin across the entire population then establishes the strong and weak connections between neurons in the observed population (Garofalo et al., 2009).

1.6.2   Granger Causality

Zhou et al., 2014 uses Granger Causality as the primary method of inferring connectivity of conductance-based integrate-and-fire neuron models; the analysis method states that if the variance in prediction error for a particular time series is reduced by incorporating knowledge of another time series, then the second time series has some causal effect on the first time series. In other words, if incorporating information about event X allows prediction of event Y beyond prediction concerning event Y without any additional information, then event X and event Y are causally related. In brief, the researchers demonstrate that using Granger Causality allows the construction of a causality matrix, which can then be mapped to the structural connectivity matrix of the population and be observed for relationships between the activity and structure of the network.

1.6.3   Transfer Entropy

Stetter et al., 2012, incorporates information theory as a reconstruction method from calcium imaging data. This particular method of reconstruction focused on in vitro calcium imaging fluorescence levels, with a slightly variant version of the Generalized Transfer Entropy formula:

$$TE_{Y->X}(\hat{g}) = \sum P(x_{n+1}, x_x^k, y_{n+1}^k | g_{n+1} < \hat{g}) log \frac{P(x_{n+1} | x_n, y_{n+1}^k, g_{n+1} < \hat{g}}{P(x_{n+1} | x_n^k, g_{n+1} < \hat{g}}$$

The major difference between the Generalized Transfer Entropy formula and the presented formula is the presence of $\hat{g}$, a predefined threshold of fluorescence, where g_t is the average fluorescence of the network at a particular time t.

The researchers use Transfer Entropy to evaluate the information transfer, where information transfer can be understood as how likely the activity of neuron Y indicates the activity in neuron X, between all possible directed pairs of neurons in the network. Afterwards, the researchers use a threshold Transfer Entropy to prune the the connections with the lowest values of information transfer, and reconstruct the network based on the remaining neurons, finding Transfer Entropy

to reconstruct network properties more accurately than previous reconstruction methods, and at varying levels of visual noise in the data, or light scattering.

1.7 The Relevance of Advances in Machine Learning

The ~~story~~ ~~concerning the invention and development of machine learning is one of constant juxtapositions with human intelligence~~. For example, the perhaps one of the most famous early experiments in artificial intelligence research is the Turing Test. The Turing Test, devised by Alan Turing, was originally named "The Imitation Game" by Turing in the 1950 paper "Computing Machinery and Intelligence". The experiment was devised with the proposed definition of artificial intelligence as the ability of a machine to replace a human counterpart in repeated rounds of questioning and answering; in other words, is the machine capable of imitating a human to the extent that participants are fooled by its answers? The performance evaluation of the machine is defined as a comparison with human intelligence, and as an antagonist to human interaction. Naturally, in the consistent comparison with human intelligence as benchmarks for machine intelligence, artificial intelligence research eventually developed methods of machine learning loosely based in the fundamental biological unit of human intelligence: the neuron.

As discussed previously, neurons are the fundamental units that allow what we understand to be human intelligence. As discussed by Steels in the paper "Fifty Years of AI: From Symbols to Embodiment", the field transitioned through several methods and approaches to AI before arriving at the neural network in the 1980s (Steels, 2007). These neural networks were developed with the intent to model the biological mechanisms of the human brain as closely as possible, primarily the neurons, which the nervous system is composed of. Even in the short history of neural networks, the method has transitioned through varying degrees of discovery and standardization concerning their usage and applicability.

1.8 Supervised and Unsupervised Learning

While the studies of machine learning have developed a variety of methods to encompass an ever-growing scope of questions to answer, the methods and questions fall into one of two categorizations: supervised and unsupervised learning. Supervised learning methods rely on the "completeness" of a data set, in which all inputs have correspondingly labeled outputs. Therefore, the output of a

supervised learning algorithm is similar in type to the actual outputs Y presented in the training data set for every X; in other words, there is a corresponding dependent output on the independent input. The natures of the inputs and outputs are variable, and need not necessarily be of the same type; for example, an input of an image can result in a categorization of the image contents, such as "dog" or "human". They can also be numerical, such as a prediction of grade based on the input amount of time studying (Hastie et al., 2009). In these two examples, the prior is an instance of qualitative, or categorical, prediction, while the latter is a quantitative, or regression, prediction.

Unsupervised learning differs in that there is no input-output; while there are X labels, there are no corresponding Y labels. Some neural networks fall under this classification of algorithms; for example, Pandarinath et al. 2017, introduces an algorithm that uses sequential auto-encoders to infer underlying patterns of spike trains. Auto-encoders are one example of unsupervised learning, where the network receives an input X, attempts to represent underlying patterns in the data, and recreate the input as the network's output.

1.9   Artificial Neural Networks

As discussed, neural networks are based on the morphology of human brains, and the neurons that the brain is composed of. These networks are composed of some number of nodes, or neurons, that are connected to each other in some fashion, depending on the task the particular network is designed for. These nodes are typically categorized into one of three layers: input, hidden, and output layers. Neurons of the input layer have no predecessor neurons, and neurons of the output layers have no following neurons; instead the the input neurons receive input information of a particular data set, and the output neurons displayed the expected outputs based on the inputs to the network and the corresponding hidden layers.

The general theory behind Artificial Neural Networks can be described as a metaphor to learning; just students prepare for exams by thoroughly studying and applying knowledge repeatedly prior to the exam, neural networks typically train on large data sets by taking an input X, and producing some inferred output Y, then comparing to the actual output that is provided by the corresponding input in the data set to calculate the error between the prediction and the true output reflected in the data set. This data set is referred to as the "training set", on which the neural network metaphorically prepares for the exam. The goal of this training is to adapt the system to

handle situations that are not contained within the training set, and predict these outputs with accuracy based on the training information provided to the network (Werbos, 1990).

1.9.1 Gradient Descent

The theory leading to the development of Gradient Descent dates back to the 1950s, proposed by Robbins and Monro in *A Stochastic Approximation Method* (Robbins and Monro, 1951; Bottou et al., 2018). Regarded as one of the notable developments in the field of machine learning, the stochastic approximation method detailed in the paper is a procedure for finding the root of an unknown function, $M(x)$, with the assumption that the function is monotonic, i.e. the first derivative of the function does not change signs (Robbins and Monro, 1951). The work of Robbins and Monro in this paper, along with additional works, marked the beginning of the field of stochastic approximation, which studies recursive and iterative algorithms of optimization problems when the data available is subject to noise (Bottou et al., 2018). Therefore, the field of stochastic approximation has had a major impact on the development of methods applied to the modern approaches to machine learning, such as neural networks (Bottou, 1991; Bottou et al., 2018). Developments in the field of stochastic approximation eventually led to application in machine learning. In the current field of machine learning, gradient descent stands as one of the most popular methods of optimization in neural networks, with a multitude of optimizations on the gradient descent method, such as gradient descent with momentum, RMSProp, Adam, applied to neural networks (Ruder, 2016).

The three primary methods of gradient descent are batch gradient descent, stochastic gradient descent, and mini-batch gradient descent (Ruder, 2016). The three methods differ primarily by the method in which the parameters of the model are updated. Batch gradient descent performs a *single* parameter update based on the gradient calculated from the *entire* dataset, while stochastic gradient descent performs the parameter update for training example with input X_i and corresponding label Y_i (Ruder, 2016). Both methods have corresponding flaws, both in theory and in application. The batch gradient descent method faces challenges in updating the model when new examples are added post-parameter updating, and must recalculate the gradient of the entire dataset once the new example is included to the dataset. Additionally, as the gradient for the entire dataset must be computed prior to a single update step, batch training on larger datasets is significantly slower

than stochastic gradient descent training (Ruder, 2016). One challenge with stochastic gradient descent lies in the tendency to change parameters and "overshoot" the optimized parametric values of the model, resulting in a slower convergences (if convergences is reached at all) (Ruder, 2016; Bottou et al., 2018). This challenge has specifically been approached via the gradient descent with momentum algorithm, which ensures that the gradient always moves towards a convergence (Ruder, 2016; Bottou et al., 2018). Here, we employ a model with basic stochastic gradient descent as the learning method.

1.9.2   Gradient Descent: Definition

The entire discussion of gradient descent focuses on parameter updating based on some *gradient*. The term gradient holds many definitions, thought the simplest way to think of a gradient is as a slope of a function. However, we can elaborate on this definition, as constructed by Kevin Gurney in *An Introduction to Neural Networks* (Gurney, 2004, p.82 -85). For example, take a function y such that y is a function of x, or $y = y(x)$. We wish to find an x_0 such that $y(x_0)$ is the minimum, or lowest output value, of the function. We denote x_i to be our current value for x. If a higher value of x_i results in a lower value of y, then we want to continue increasing x. We define this change as $\Delta x > 0$. Therefore, a negative x with a lower value of y can be defined as $\Delta x < 0$. Here, we arrive at the definition of a slope, as given by differential calculus; for a given point x_i, the slope of the function at x_i is the derivative of the function at that point. We represent the derivative of y with respect to x as

$$\frac{\Delta y}{\Delta x}$$

From there, we can manipulate the function by multiplying it with Δx produces

$$\Delta y = (\frac{\Delta y}{\Delta x})\Delta x$$

As we reduce Δx, $dy \approx \Delta y$. Now, we suppose that $\Delta x = -\alpha(\frac{dy}{dx})$, where α is some constant such that $\alpha > 0$ (sometimes referred to as the *learning rate*), and small enough so $dy \approx \Delta y$. If we substitute Δx, we arrive at

$$dy = -\alpha(\frac{dy}{dx})^2$$

which indicates that y will keep traveling towards the minimal point. We generalize $\Delta x = -\alpha(\frac{dy}{dx})$ to multivariate functions to arrive at

$$\Delta x_i = -\alpha(\frac{\partial y}{\partial x_i})$$

. Repeating this calculation for all variables results in gradient descent (Gurney, 2004, p.82 - 85). Next, we observe how to calculate the gradient via backpropagation.

1.9.3   Backpropagation in Neural Networks

Backpropagation is one of the most widely applied techniques in the applications of artificial neural networks. Developed by Paul Werbos in the 1970s, backpropagation is the primarily used method of learning in neural networks (Widrow et al., 1990). The method is so named because the updating of weights at every layer begins at the final layer, and propagates backwards to every node and weight until all weights of all nodes in each layer have been adjusted for the calculated error in the network. To fully understand backpropagation, we begin with an example of a neural network of the following layout.

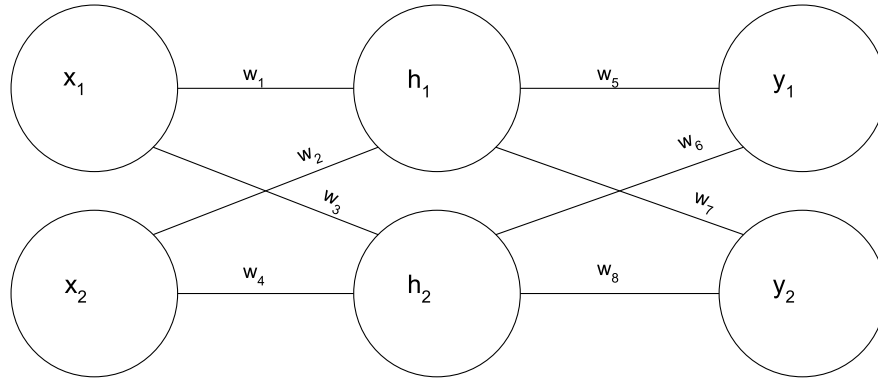**Figure 2:** Simple, Feedforward Neural Network. x denotes an input layer node, h a hidden layer node and y an output layer node. w denotes a connection from a node to the node in the next layer, from left to right.

In the simple, feedforward neural network (Figure 2), there is a single input layer, hidden layer, and output layer. Each layer is composed of several nodes with some activation function; in the

simplest models, where threshold linear units (TLU) are used as the nodes, the activation is a threshold. To predict the output y_1, we first propagate the x_1 and x_2 input values forward, via the connections from the input layer to the output later, and multiply by the corresponding weight. Therefore, the value incoming to h_1 can be represented as $\alpha = x_1 * w_1 + x_2 * w_2$. In the TLU, the value is then thresholded via an arbitrary threshold θ, such that

$$h_1 = \begin{cases} 0 & \alpha \leq \theta \\ 1 & \alpha > \theta \end{cases}$$

The activation of the TLU is loosely based on the circuitry and behavior of biological neurons, where the incoming connections to an node reflect dendritic connections of a neuron, and the threshold behavior reflects the all-or-nothing nature of an action potential, and corresponding signal propagation (Gurney, 2014, 31; Steels, 2007). However, other activation functions are commonly used, such as the sigmoid function (Gurney, 2014, 35-36). We calculate in a similar fashion for h_2, using the weights at w_3 and w_4 (Gurney, 2014, 29-30; Hecht-Nielson, 1989). With the newly calculated values at the hidden layer, we perform the same operations on the values to find the prediction values in the output layer. For example, $y_1 = h_1 * w5 + h_2 * w_6$, and y_2 follows a similar calculation, with weights w_7 and w_8 (Gurney, 2014, 29-30; Hecht-Nielson, 1989).

Once all output node values are calculated, the forward-pass is complete, and the backward-pass, or backpropagation, shifts the network along the gradient towards convergence of the error and weights. In the presentation of gradient descent presented earlier, we arrived at the definition as an iterative process of the function

$$\Delta x_i = -\alpha(\frac{\partial y}{\partial x_i})$$

(Gurney, 2014, 82-85). However, we now apply the function as a minimization process of the *error*, with respect to the *weights* of the neural network. Therefore, the change in weight during a backpropagation step can be represented as

$$\Delta w_{ij} = -\alpha(\frac{\partial E}{\partial w_{ij}})$$

. The target function to minimize is now the cost function, and the variables to be changed are all weights in the neural network. At the backpropagation step for updating the weights between

the output layer and the prior hidden layer in our example simple feedforward neural network, the chain rule is applied on $\frac{\partial E}{\partial w_{ij}}$, which expands to

$$\frac{\partial E}{\partial w_{ij}} = \frac{\partial E}{\partial y_j} * \frac{\partial y_j}{\partial I_j} * \frac{\partial I_j}{\partial w_{ij}}$$

where i denotes the source node, j the target node. The function for finding the change in error with respect to (w.r.t) a change in particular weights is expanded to three calculations: the change in error w.r.t. change in the output of the activation function, the change in the output of the activation w.r.t change in the inputs to the activation function, and the change in the inputs of the activation w.r.t. change in w_{ij} (Gurney, 2004, 89-91; Hecht-Nielson, 1989). The value these calculations evaluate to depends on the error calculation method, the activation function, and how the inputs to the calculation function are calculated; using a TLU in place of a sigmoid function will result in a different Δw_{ij}.

Backpropagation between the hidden and input layers of the follow a similar approach, with a difference in the calculation of error; since we are now calculating for a hidden node, with forward connections to output nodes in the output layer, each hidden neuron contributes to the error contribution of several output nodes. Therefore, we must sum the error contribution over all nodes that the the hidden node contributes to, resulting in

$$\frac{\partial E}{\partial w_{ij}} = \sum_{k=I_i} \frac{\partial E_k}{\partial y_j} * \frac{\partial y_j}{\partial I_j} * \frac{\partial I_j}{\partial w_{ij}}$$

where I_i is the set of all neurons in the next forward layer that receive input from the hidden node k that we are backpropagating from (Gurney, 2004, p.100-101; Hecht-Nielson, 1989). Both methods are applied during backpropagation of a neural network, depending on the weight being updated. $\frac{\partial E}{\partial w_{ij}}$ is calculated for all w_{ij} between the output and hidden layers, for every training step, typically until error converges and does not minimize further, successfully performing gradient descent on the error.

1.10   NEST: Generating Training Data

There are several reasons for generating simulated calcium imaging data for the purposes of network reconstruction. First, generation of simulated calcium imaging data allows for benchmarking of the reconstruction methods employed. In typical calcium imaging data, the ground truth is not known,

resulting in a lack of comparison between the reconstructed network and the network targeted for reconstruction. By generating simulated networks and recreating calcium imaging data, we ensure access to the ground truth for comparison with the model. Simulation of training data also permits programming of particular characteristics to the network, and observing the changes of this reconstruction in both the simulated data and the reconstruction of these networks.

Machine learning methods are typically trained on some prior data set. Simulation of calcium imaging data provides an easily accessible method of generating data for training and testing the machine learning based model, due to unconstrained and unrestricted access to data, before allowing the model to analyze recorded data that would be ideally used as testing data. Additionally, including a training set ensures that the algorithm is able to remain generalized; that is, the algorithm does not learn to represent that single data set exceptionally well, and fail when a different pattern is presented to the algorithm.

The simulations presented here are performed in NEST simulator, a tool maintained by the NEST initiative (Kunkel et al., 2017). The NEST simulator was selected for the purpose of simulations that maintain biological realism and complexity, with emphasis on simulation of large neuronal networks. The advantage NEST has over other simulators is the capability to simulate large networks with varying facets, such as synapse and neuron types, while retaining accurate representation of the individual neurons.
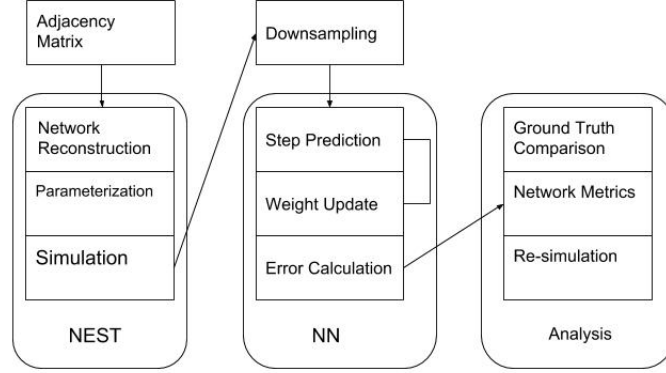
2   Methods

Figure 3: Experimental Pipeline. We start with a pre-generated adjacency matrix detailing the connections of a population of neurons, and pass it to the NEST simulator program. The NEST simulator reconstructs the network defined by the matrix; at this stage, Poisson noise is added to the population via a connection from a 'noise generator' NEST object to all neurons in the population. The simulation is then run for 10000 time steps (milliseconds), and the generated data is output as a spike time matrix of n x t dimensionality, n = population size and t = time steps. The output is then downsampled to reflect realistic calcium imaging frame duration of 10 ms, reducing the data set to t = time steps/10.

2.1   Simulation of Neurons for Spike Train Generation

The NEST simulator is used for the purposes of generating spike train data. NEST Izhikevich neurons are used as the model neurons, due to the increased complexity over leaky integrate-and-fire neurons, and the reduced computational complexity over models of significantly more numerous compartment models, such as the Hodgkin-Huxley models (Brette, 2015). NEST implementation dynamics of Izchikevich neurons are provided by the following:

$$dv/dt = 0.04v^2 + 5v + 140 - u + I$$

$$du/dt = a(bv - u)$$

$$\text{if } v >= V_{th} : \{$$

$$v = c$$

$$u = u + d\}$$

where v represents the membrane potential of the neuron and u the membrane recovery variable. The membrane recovery variable captures the responses of K^+ and Na^+, and is a source of negative feedback to v. Coefficients for change in membrane potential, are based on scale, with membrane potential at mV and time as ms, as are a and b. I is the input current to the neuron, and c and d are the post-spike reset values of the neuron (Kunkel et al., 2017, Izhikevich et al., 2004).

To simulate a population of neurons with n population size over t time, a file containing an n x n adjacency matrix is provided to the simulation program, which then creates a NEST neuron population with the exact number of neurons and connections between the neurons in the population, using the corresponding weight of the connection stored in the adjacency matrix. Interactions with neurons in NEST must be achieved through the creation of new node objects, made to represent and achieve the results of physical instruments and devices; therefore, we create a Poisson generator node to add noise to the population, and connect a spike detector node to record all spikes in the population during simulation. The population is then recorded over 10000 simulation steps, or 10000 ms. The corresponding output of the simulation is converted to a matrix of n x t dimensionality. The simulation is repeated to produce 100 spike trains from one adjacency matrix.

Post-simulation, all data is downsampled from 10,000 ms to 1,000 ms, corresponding to the 10 ms frame rate of calcium imaging. Downsampling is performed by observing consecutive reading frames of size 10 time steps (ms), and checking for occurrences of spikes within the 10 frames. If one or more spikes occur within the frame for a particular neuron, a single spike is recorded for the neuron; otherwise, no spikes are recorded for the neuron. The downsampling produces a dataset that resembles a similar time step size of 10 ms to the *in-vivo* Xenopus Laevis calcium imaging data available.
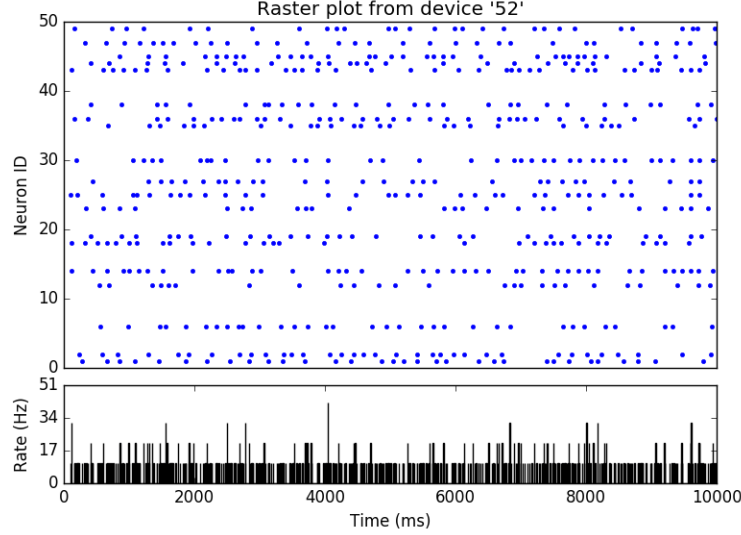
Figure 4: Raster Plot via NEST Simulator. The plot is generated by simulating a population of 50 neurons over 10000 time steps (ms), and graphically represents two distinct arrays output by the simulation: one array consisting of neuron IDs in the population, and another array with the corresponding spike times of the spiking neurons stored in the indices of the former array. The NEST simulator connects each neuron based on the input adjacency matrix and attaches additional noise and spike detection objects to every neuron in the population. Device 52 is the NEST spike detection object; all neurons are connected by the NEST simulation program for the purposes of spike detection. Device 51 is the noise generator object, and Devices 1-50 are the neurons in the population.

2.2   Machine Learning Model

2.2.1   Base Model

The model presented contains only two layers: an input layer and a hidden layer. We attempt to restrict the number of layers to a single layer, in order to extract a single set of weights that can be understood as the adjacency matrix reflecting the population of neurons from which the spike-train originates. The base model is a two-layer network with the squared error of the form

$$E_{total} = \sum \frac{1}{2}(target - prediction)^2$$

as the error function, where the target is the y label to a corresponding x input, and prediction is the output of the model after one prediction step (Werbos, 1990; Gurney, 2004, p.86-66; Bohte et al., 2002). The base model has a simple structure of n x 1 dimensionality in each layer, with 2 layers and n x n weights connecting them.

First, a single time step is provided from an t x n dimensional matrix, where t is the number

of time steps, as an 1 x n array, where each n is a neuron id corresponding to a specific neuron in the population. The time step is matrix multiplied by the weight matrix of n x n, resulting in the prediction array of 1 x n. Each value in the prediction array is passed to the sigmoid activation function

$$f(x) = \frac{1}{1 + e^{-x}}$$

and updated as the prediction of the active and inactive neurons in the next time step. Therefore, the backpropagation step calculates the weight changes

$$\frac{\partial E}{\partial w_{ij}} = \frac{\partial E}{\partial y_j} * \frac{\partial y_j}{\partial I_j} * \frac{\partial I_j}{\partial w_{ij}}$$

where the partial derivative of the error w.r.t the prediction y_j and target $\hat{y}_j$ expands to

$$\frac{\partial E}{\partial y_j} = -(\hat{y}_j - y_j)$$

due to the summation in the error function; all other predictions are held constant, which results in a zero derivative for the remainder of the summation outside of y_j. The partial derivative of the output of the activation function y_j w.r.t. the input I_j, or the results of the first matrix multiplication, evaluates to

$$\frac{\partial y_j}{\partial I_j} = \frac{e^{I_j}}{(1 + e^{I_j})^2} = y_j * (1 - y_j)$$

Finally, the partial derivative of the input to the activation function I_j w.r.t. the weight being updated w_{ij} is

$$\frac{\partial I_j}{\partial w_{ij}} = 1 * x_i * w_{ij}^{1-1} = x_i$$

. Therefore, the full learning rule applied in this model is

$$\frac{\partial E}{\partial w_{ij}} = -(\hat{y}_j - y_j) * (y_j * (1 - y_j)) * x_i$$

. At every time step, the learning rule is applied to the current input and predicted next time step, and each traversal across the entire dataset is an iteration of the learning process.

Algorithm 1: Base Model

Initialize the weight matrix of n x n size with random values 0-1.

Initialize dataset as spike-time matrix

i = A time step in the spike-time matrix

for i < number of spike Times **do**

    Calculate dataset[i]*weights $\rightarrow$ outputs (1 x n)

    Multiply each value in outputs by the activation function

    return the 1 x n dimensional array of predictions of activity in the next time step

    j = index of the source neuron in the weight matrix

    k = index of the target neuron in the weight matrix

    w_{jk} = a weight in the weight matrix corresponding to indices j,k

    for w_{jk} in the weight matrix **do**

        Calculate $\Delta w_{jk} = \frac{\partial E}{\partial w_{jk}}$

        Update the weight via $w_{jk} = w_{jk} - \alpha(\Delta w_{jk})$

Generate a new set of predictions P' with the calculated Matrix

Calculate the mean squared error between P'[0:length-1] and dataset[1:length]

2.2.2 Variable Activation Function Model

The variable activation function model contains two additional sets of values in two separate n x 1 dimensional arrays, where n is the size of the population of observed neurons. Each value in the matrix corresponds to a particular node in the output layer of the same index. Therefore, the activation function is modified to a general logistic function of the form

$$f(x) = \frac{1}{1 + e^{-a(x-b)}}$$

where a_j and b_j are the values corresponding to the unique steepness, or shape, and center, defined as the value at which the second derivative of the function changes signs, of the activation function for target output node y_j, allowing for a distinct activation function for each output node. The error is backpropagated in a similar fashion to the weights between the input and output layers of the model, and simultaneous to the weight updating step. To update the steepness of the of output y_j, we calculate Δa_j as

$$\Delta a_j = \frac{\partial E}{\partial a_j} = \frac{\partial E}{\partial y_j} * \frac{\partial y_j}{\partial a_j}$$

where $\frac{\partial E}{\partial y_j}$ is evaluated as in the base model, and the partial derivative of the output y_j w.r.t logistic function steepness a_j, $\frac{\partial y_j}{\partial a_j}$, is

$$\frac{\partial y_j}{\partial a_j} = \frac{e^{-a_j(x-b_j)}(b_j - x)}{(1 + e^{-a_j(x-b_j)})^2}$$

, where x is the input to the activation function. The change of the logistic function center at the update step is given by

$$\Delta b_j = \frac{\partial E}{\partial b_j} = \frac{\partial E}{\partial y_j} * \frac{\partial y_j}{\partial a_j}$$

where the partial derivative of the output y_j w.r.t logistic function center b_j, $\frac{\partial y_j}{\partial b_j}$ is calculated as

$$\frac{\partial y_j}{\partial b_j} = \frac{a_j e^{-a_j(x-b_j)}}{(1 + e^{-a_j(x-b_j)})^2}$$

Algorithm 2: Variable Activation Function Model

Initialize the weight matrix of n x n size with random values 0-1.

Initialize dataset as spike-time matrix

i = A time step in the spike-time matrix

for i < number of spike Times **do**

> Calculate dataset[i]*weights $\rightarrow$ outputs (1 x n)
>
> Multiply each value in outputs by the activation function
>
> return the 1 x n dimensional array of predictions of activity in the next time step
>
> j = index of the source neuron in the weight matrix
>
> k = index of the target neuron in the weight matrix
>
> w_{jk} = a weight in the weight matrix corresponding to indices j,k
>
> **for** w_{jk} in the weight matrix **do**
>
> > Calculate $\Delta w_{jk} = \frac{\partial E}{\partial w_{jk}}$
> >
> > Update the weight via $w_{jk} = w_{jk} - \alpha(\Delta w_{jk})$
>
> **for** a_j *in the steepness matrix* **do**
>
> > Calculate $\Delta a_j = \frac{\partial E}{\partial a_j}$, $\Delta b_j = \frac{\partial E}{\partial b_j}$
> >
> > Update the steepness and center via $a_j = a_j - \alpha(\Delta a_j)$, $b_j = b_j - \alpha(\Delta b_j)$

Generate a new set of predictions P' with the calculated Matrix

Calculate the mean squared error between P'[0:length-1] and dataset[1:length]

2.3   Cross-Correlation

We compare the performance of the model to the cross-correlation method of inferring connectivity. Cross-correlograms here are produced using the *elephant* and *neo* python packages; these packages assist in calculating the cross-correlation matrix by producing cross-correlograms for the input spike trains. The cross-correlogram method of extracting spike-train correlations compares the spike times of a reference train to a target train. Different time steps within a defined window are observed in the target train, using a spike in the reference train as the origin. For each spike in the reference spike train, the spikes in the target spike train are counted in the bins according to the time lag, where the origin time 0 is set to the time of the reference spike in the reference spike train. The final cross-correlation analysis compares over 100 distinct simulated spike time datasets across a population of 10 neurons, with window size [-10,10], as displayed in Figure 5f.

To designate the highest probability of connections in spike trains from a spike time matrix, we calculate the cross-correlogram for each combination of spike train in the spike time matrix, and find the time bin with the largest amount of counts. This count value is calculated for all combinations of neurons in the spike time matrix, and normalize the values between 0 and 1. Since auto-correlograms represent self-connections and contain the highest counts, where each auto-correlogram max value is equivalent to the number of spikes occuring in the spike train of the neuron, we ignore the auto-correlograms when normalizing the adjacency matrix.
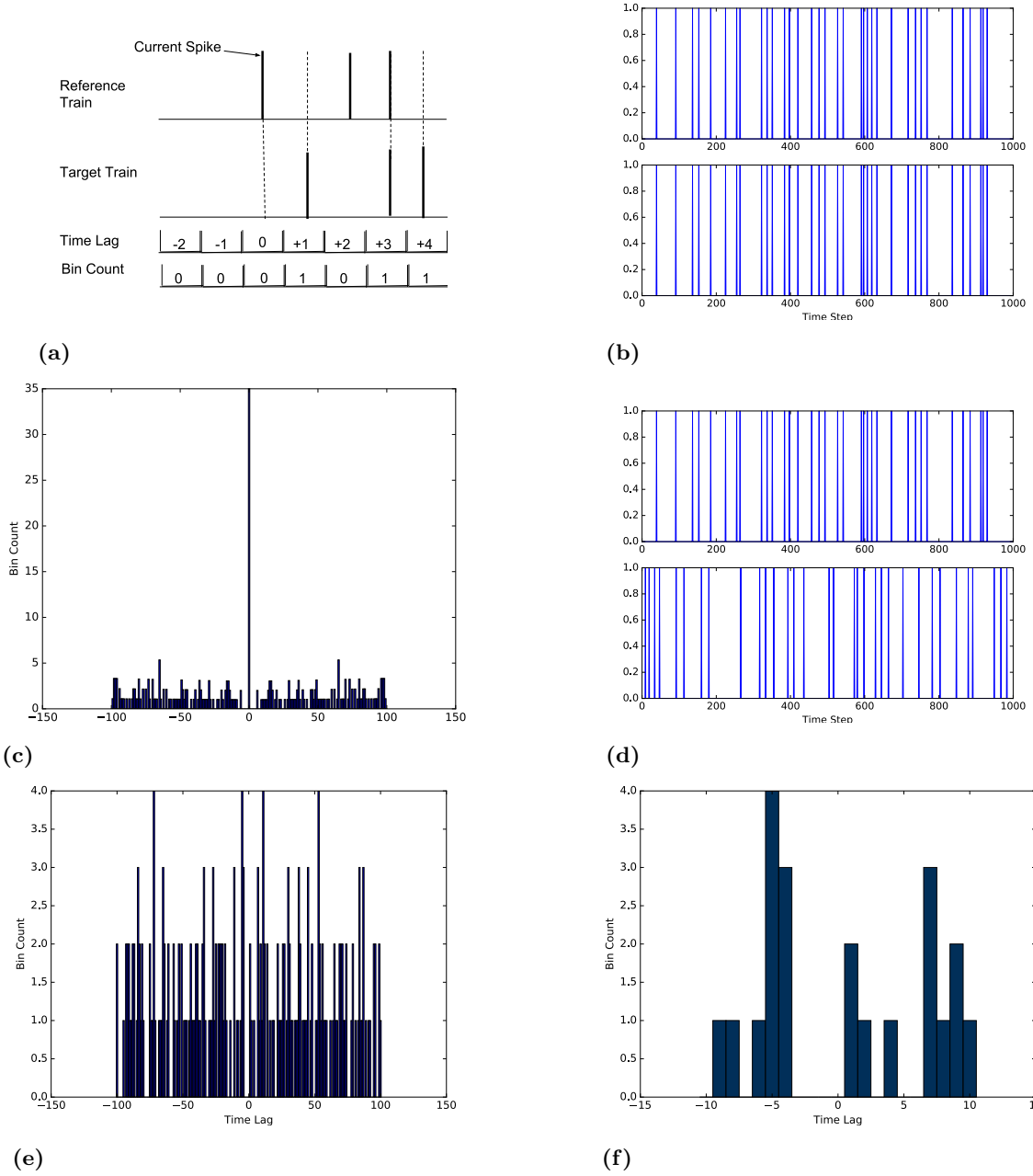
Figure 5: Cross-Correlation Histogram (Cross-correlogram) Procedure and Example. (a) The cross-correlogram method of relating spike-trains. A spike is selected and designated as the reference point. If a spike appears in the target train at a particular time lag, the value for that bin is incremented.(b)An example autocorrelation spike-train. The top and bottom spike trains are the same spike-train; all spikes align.(c) The autocorrelogram calculated from (b), with a window range of [-100,100]. In an autocorrelation, the highest bin count should be equivalent to the number of spikes in the observed train, and the highest bin is at time lag 0.(d) Two distinct spike-trains. Note the periodic nature of the histogram, identified in (f) (e)Cross-correlogram of (d). (f)Cross-correlogram of (d), window range of [-10,10].

2.4   Degree Distribution, Spike Rate, and Binary Spike Time Data

The *degree* of a node is the number of edges, or connections, to that node (Costa et al., 2005; Hernandez and Miegham, 2011). The degree distribution is a distribution of probabilities. The probabilities are of a node n containing degree k number of connections, and is given by

$$Pr[D = k] = \frac{d_k}{N}$$

where d_k denotes the number of nodes with degree k and N is the population size (Hernandez and Miegham, 2011). Indegrees, outdegrees, and total degrees for each node are calculated from adjacency matrices of the population, where the rows indicate an outgoing connection and columns indicating incoming connections. The total degree is obtained by adding the indegrees and out-degrees. The total degree distribution, indegree distribution, and outdegree distribution are then calculated for the adjacency matrix.

To obtain binary values from probability value representations present in the *Xenopus Laevis* calcium imaging data, all non-zero values are denoted as spikes. In the case of the resultant spike time matrices produced by the machine learning models, the matrices are normalized between 0 and 1, and thresholded at 0.5, where values greater than or equal to 0.5 indicate a spike, and values below indicate no spiking. Spike rates from the prediction spike time matrices are inversely calculated in the variable activation function model, where a 0 indicates spiking and 1 indicates no spiking.

3   Results

3.1   Error

3.1.1   Two Time Step Convergence

We first run the model across two time steps, with at least a single observed spike difference between the two steps, to observe the rate of error convergence and capability of the model to predict from a single time step to the next time step. Error is calculated between the prediction of the model and the known target time step using mean squared error. Figure 6a and Figure 6c demonstrate the subcase of the running the model on two time steps and observing the error after each iteration, over 100 iterations, where the two time steps feature a single spike at the input time step and a single spike in the output time step. The other subcases present in the training data were combinations of up to four spikes occurring in any given time step. In the simulated spiking of a $n = 10$, across 100 distinct simulations, 73,481 time steps had a spike count of zero, 22,499 contained a single spike, 3568 contained two spikes, 427 contained three spikes, and 25 time steps contained four spikes, indicating 16 possible subcases for the number of spikes in the input and output time steps. However, some subcases, such as two consecutive time steps containing four spikes each, did not appear. The two models each behaved differently when training on different subcases, as indicated by the wide standard deviation bars in Figure 6b and Figure 6d, where each plot contains information concerning 10 of the 16 possible subcases. These subcases all occurred within the same spike time dataset. The wide standard deviation bars indicate a high variability in the model training error of Figure 6b and Figure 6d, where 10 different subcase errors are plotted, indicating that performance of both models vary, depending on which time steps the model was being trained on.
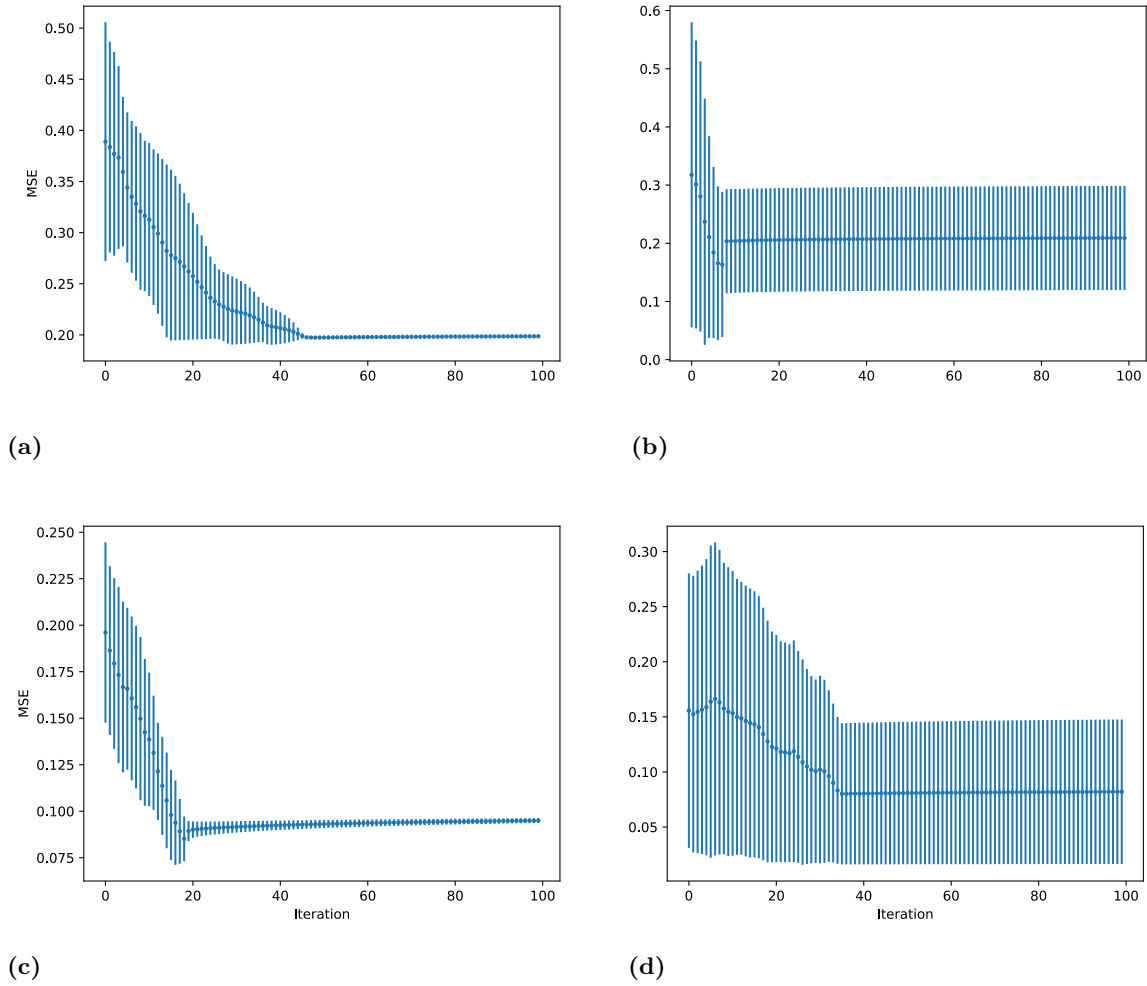
Figure 6: Error Convergence of Model On Two Consecutive Time Steps. Each plot represents an average of 10 separate runs of the model, each run lasting 100 iterations. (a)Error Convergence on Variable Activation Function Model. The model was trained on a selected time step, where the first time step contained a single spike, and the following contained a single spike in a different neuron (subcase [1,1]). (b)Average error across ten separate runs of differing subcases with distinct spiking patterns. The subcases are as follows: [0,0], [0,1], [0,2], [0,3], [1,1], [1,2], [2,0], [2,1], [2,2], and [3,0], where the first value is the number of spikes in the input time step, followed by the number of spikes in the output time step. (c) Error calculation using the identical time step to (a), with the base model.(d) Error calculation using the identical distinct time steps to (b), with the base model.

3.2   Degree Distribution

Degree distribution analysis was performed on the final weight matrices produced by the models for both simulated and *Xenopus Laevis* calcium imaging recordings, with a threshold of 0.50, with population sizes of 10 and 50 for the simulated data adjacency matrices; in *Xenopus* calcium imaging

data, the population size varied, depending on the recording. The average degree distributions of the predicted adjacency matrices from simulated data are calculated by averaging the degree distribution over all predictions. Calculations of the average degree distribution from the calcium imaging data predictions are performed in the same fashion, over 6 predicted adjacency matrices from 6 *in-vivo* calcium imaging recordings from *Xenopus Laevis*.
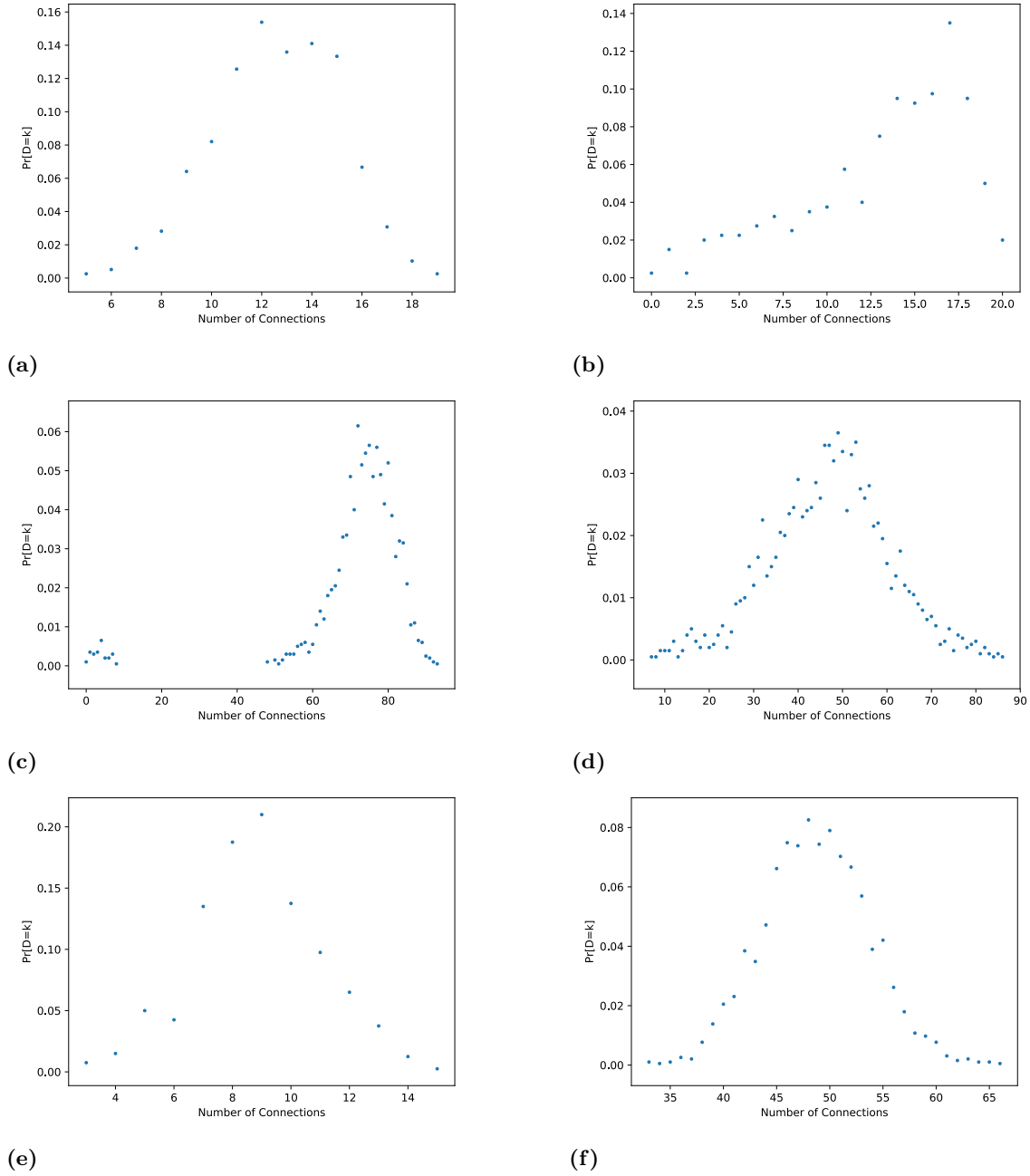
(a)

(b)

(c)

(d)

(e)

(f)

Figure 7: Average Degree Distribution in Simulated Data Predictions. (a)Average degree distribution of the simulated data from population size 10, averaged across the resulting adjacency matrices of the variable activation function model across 40 simulated spike time matrices.(b)Average degree distribution from base model. (c) Average degree distribution of the simulated data from population size 50, averaged across the resulting adjacency matrices of the variable activation function model produced from 40 simulated spike time matrices.(d) Average degree distribution of the simulated data from population size 50, averaged across predictions from the base model produced from 40 simulated spike time matrices.(e)(f) Calculated average degree distributions across 40 randomly generated networks of population size 10 and 50, respectively.
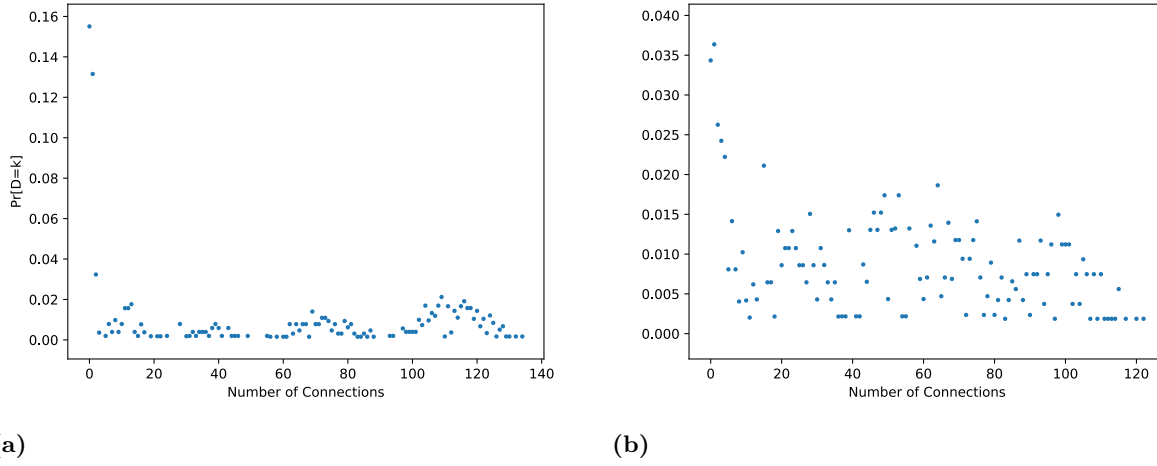
(a)

(b)

Figure 8: Average Degree Distribution in *Xenopus* Calcium Imaging Data Predictions. (a) The average degree distribution of the resulting variable activation model prediction adjacency matrix from 6 *in-vivo* recordings of calcium imaging data from Xenopus Laevis (b) Distribution of the adjacency matrices produced from the base model, from the same datasets as (a).

The average degree distributions differed between the simulation predicted adjacencies and the calcium imaging adjacencies; where the simulated data produced an average degree distribution resembling a normal distribution, the average degree distribution calculated at the same threshold value of 0.5 from the calcium imaging data resembles a power-law distribution, in both the base model and the variable activation model.

3.3 ROC

The receiver operating characteristic (ROC) curve is a measure of performance for testing the accuracy of models where the ground truth underlying the data is available for comparison. The receiver operating characteristic plots the true positive rate (TPR) against the false positive rate (FPR) to evaluate the performance of the model on the simulated data sets (Garofalo et al., 2009). The TPR is evaluated according to

$$TPR = \frac{TP}{TP + FN}$$

where the FPR is evaluated according to

$$FPR = \frac{FP}{FP + TN}$$

where TP, FP, TN and FN are defined in the contingency table (Figure 9)

		True Condition	
		Positive	Negative
Predicted Condition	Positive	TP	FP
	Negative	FN	TN

Figure 9: Contingency Table. The designations of true positive (TP), false positive (FP), false negative (FN), and true negative (TN). For example, a positive appearing in the true condition and a positive appearing in the predicted condition is a TP.

In the adjacency matrices, positives are defined as a value of "1" and negative as "0". When comparing between two matrices, a positive in the predicted matrix at P_{ij} and a positive in the ground truth matrix at M_{ij} indicate a true positive. TPRs and FPRs are calculated for cross-correlation, the base model, and the variable activation function model.

ROC curves are constructed by varying some parameter and observing the resulting TPRs and FPRs. In the ROC curve below, we simply increase the threshold at which a normalized value in the predicted weight matrix is counted as a connection. Starting from a threshold of 0, which allows all possible connections, we increase by 0.01 at every iteration, until 1, at which point there are no longer any connections in the predicted matrix. At every threshold, the TPRs and FPRs are calculated. In the case of the base model and the activation function model, the TPRs and FPRs at every threshold are calculated for 40 distinct datasets on which the models were trained. The TPRs and FPRs for every dataset, at every threshold, is accumulated. Redundant TPR and FPR calculations are removed before plotting and analysis; plotting the redundant points would result in overlapping points and a weighted area under the curve (AUC). ROC curves for models are plotted against random guessing, represented as a linear relationship between TPR and FPR, with an AUC of 0.5. Cross-correlation ROC is calculated across 100 distinct simulated datasets, with TPR and FPR accumulated across all datasets and redundant TPR and FPR calculations removed.
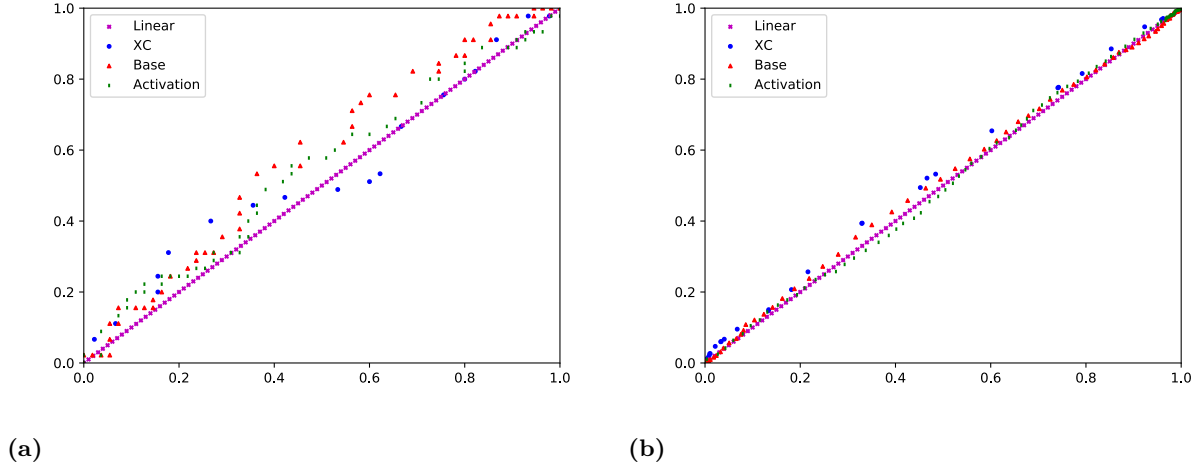
(a)

(b)

Figure 10: Receiver Operating Characteristic. The linear function depicted is random guessing, with an AUC of 0.5.(a) ROC on cross-correlations and model results from population size of 10. Activation AUC = 0.54, Base = 0.58, XC = 0.53. (b) ROC on cross-correlations and model results from population size of 50. Activation AUC = 0.49, Base = 0.51, XC = 0.53.

To better compare the curves, we calculate the AUC to describe the curve as a single value. The AUC is calculated as the integral of the ROC curve from 0 to 1, using the composite trapezoidal rule. While the accumulated ROC curves depicted above have the calculated AUC as listed in the caption, the average AUCs, calculated for every dataset from which the ROC curves are constructed, are as follows: XC = 0.46 ($\pm$ .07), Activation AUC = 0.45 ($\pm$ .09), Base AUC = 0.47 ($\pm$ .09) for population size 10, and XC = .48 ($\pm$ .01), Activation AUC = 0.44 ($\pm$ .02), Base AUC 0.49 ($\pm$ .01) for population size 50.

4 Discussion

4.1 Differences in Degree Distribution

The calculated average degree distributions of the simulated data resemble a Gaussian distribution in the cases of both models, most clearly seen in Figures 7c and 7d. The ground truth degree distributions displayed in Figures 7e and 7f are randomly generated networks, with each network generated in the same fashion as the ground truth matrices for all network simulations. While the predicted degree distribution for population size 10 from the base model is right-skewed (8b), all other distributions resemble the binomially distributed probabilities. The degree distribution of random networks is commonly described as resembling a binomial distribution, Poisson distribution, or Gaussian distribution, depending on the literature and usage (Hernandez and Meighem, 2011; Costa et al., 2005; Massobrio et al., 2015; Strogatz, 2001). In the degree distributions produced from *Xenopus* calcium imaging data, the curves do not resemble the Gaussian distribution; in both cases, the distributions resemble a power-law behavior, characterized by the higher rate of sparsely connected nodes, and the lower rate of densely connected nodes (Hernandez and Meigem, 2011; Massobrio et al., 2015). Networks that are characterized by the power-law distribution are referred to as *scale-free* networks (Eyton and Marom, 2006; Massobrio et al., 2015). This distinct connection pattern differs from that of networks that fit a Gaussian distribution, where nodes in the network tend to have a number of connections varying around an average number of connections.

While the degree distribution does not inform us about the exact manner in which the neurons in the network are connected, the distribution indicates that the model may be able to capture underlying patterns of connectivity in the population. However, whether or not the underlying connectivity pattern of neurons fits a power-law distribution is a debated topic among the neuroscience community. Some studies have indicated scale-free architectures in networks, such as in *in-vitro* cortical neuronal networks (Eyton and Moran, 2006), in rat hippocampal slices (Bonifazi et al., 2009) and in other studies of network reconstruction (Pajevic and Plenz, 2009). Additionally, a study in the *Xenopus* optic tectum indicates the scale-free acrhictecture to be a possibility; however, in this particular study, the researchers found a uniformly distributed network to be a more robust, and therefore more likely architecture. Other studies find no evidence of scale-free architectures (Stetter et al., 2012).

4.2   Model Error Convergence

When the model is run on two time steps, we observe distinct error convergence patterns, dependent on the activity of the input and target time steps. As observed in Figures 6a and 6c, the error convergence of an input spike time step containing a single spike and a target spike time step containing a single spike converges at around 20 iterations of training in the base model, and around 45 iterations of training in the variable activation function model. Furthermore, the error convergence between ten runs results in a low standard deviation. Training the model on distinct spiking patterns results in larger standard deviations; the stable standard deviations indicate that, between all distinct spiking patterns, the model generally converged at the same iteration, at widely differing values of convergence, indicating different calculations of error dependent on the spiking pattern.

4.3   Receiver Operating Characteristic and Accuracy of Model

The receiver operating characteristic curve is a metric for evaluating performance accuracy of a model. Here, we observe the ROC of performance on our cross-correlation implementation, our base model, and our variable activation function model. While the initial ROC curve of the base and activation modles with a population size 10 (figure 10a) appeared to perform better then the implementation of cross-correlation, the cross-correlation method performed worse than implementations of cross-correlation, as well as methods such as mutual information, transfer entropy applied in other studies (Garofalo et al., 2009; Stetter et al., 2012). Additionally, while the AUC calculated from averaging TPRs and FPRs across all cross-correlation results (AUC = 0.53) is higher than the linear relationship (AUC = 0.5), the average AUC calculated by determining individual AUC and averaging is slightly lower (AUC = 0.46 ($\pm$ .07). These results indicate that the base model, variable activation function model, and the cross-correlation implementation here did not perform better than any existing method applied in other studies, where cross-correlation AUC = 0.70 ($\pm$ 0.05).

5 Conclusion and Future Work

We develop a model based on methods applied in neural networks, an architecture used in machine learning, and attempt to extract the underlying connectivity of the populations of neurons by training the model on the spike-time data of these populations. While the results suggest that the model is able to capture the degree distributions of the underlying networks, the model is not able to accurately predict the connections of the population.

Due to technical limitations, analysis of calcium imaging data was performed on a sample size of 6 spike time datasets. Analysis on a larger sample size would solidify the findings of the degree distribution presented in Figure 8, and allow for a more accurate comparison with the degree distributions random networks characterized in Figure 7.

There are various possible improvements that could be made to the model. Here, we use an architecture resembling a simplified neural network, with changes to the update sequence to allow each neuron a unique activation function resembling the logistic function. Furthermore, we restrict the network to a single set of weights between the input and output layers, constraining the learning capabilities of the network. One possibility for improvement is inclusion of backpropagation methods that incorporate the timing of the spike (Bohte et al., 2002; Werbos, 1990). Such backpropagation methods are more biologically inspired than traditional neural networks; these methods are inspired by the temporal coding activity of neurons, where information is conveyed in the precise timing of a spike (Purves, 2004, 349; Bohte et al., 2002). Improving the model to account for further network dynamics of neurons would likely produce more accurate reconstructions.

6 Works Cited

1. Alberts B, Johnson A, Lewis J, et al. Molecular Biology of the Cell. 4th edition. New York: Garland Science; 2002. Ion Channels and the Electrical Properties of Membranes. Available from: https://www.ncbi.nlm.nih.gov/books/NBK26910/

2. Armstrong, C. M., & Hille, B. (1998). Voltage-Gated Ion Channels Review and Electrical Excitability Early Biophysics and Voltage Clamp Revealed Voltage-Gated Membrane Permeabilities The period from 1939 to 1952 was a heroic time in the. Neuron, 20, 371–380. https://doi.org/10.1016/S0896-6273(00)80981-2

3. Bean, B. P. (2007). The action potential in mammalian central neurons. Nature Reviews Neuroscience, 8(6), 451–465. https://doi.org/10.1038/nrn2148

4. Biswal, B., Yetkin, F. Z., Haughton, V. M., & Hyde, J. S. (1995). Functional Connectivity in the Motor Cortex of Resting. Magnetic Resonance in Medicine, 34(4), 537–541.

5. Bock, D. D., Lee, W. A., Kerlin, A. M., Andermann, M. L., Hood, G., Wetzel, A. W., . . . Reid, R. C. (2011). Network anatomy and in vivo physiology of visual cortical neurons. Nature, 471(7337), 177–182. https://doi.org/10.1038/nature09802

6. Bohte, S. M., Kok, J. N., & Poutrã, H. La. (2002). Error-backpropagation in temporally encoded networks of spiking neurons. Neurocomputing, 48, 17–37.

7. Bonifazi, P., Goldin, M., Picardo, M. A., Jorquera, I., Cattani, A., Bianconi, G., . . . Cossart, R. (2009). GABAergic hub neurons orchestrate synchrony in developing hippocampal networks. Science, 326(5958), 1419–1424. https://doi.org/10.1126/science.1175509

8. Bottou, L. (1991). Stochastic Gradient Learning in Neural Networks. Proceedings of Neuro-Nimes, EC2.

9. Bottou, L. ,Curtis, F. E. & Nocedal J. Optimization methods for largescale machine learning. arXiv:1606.04838v3, 2018.

10. Brette, R. (2015). What Is the Most Realistic Single-Compartment Model of Spike Initiation? PLoS Computational Biology. https://doi.org/10.1371/journal.pcbi.1004114

11. Brette R, Rudolph M, Carnevale T, et al. Simulation of networks of spiking neurons: A review of tools and strategies. Journal of computational neuroscience. 2007;23(3):349-398. doi:10.1007/s10827-007-0038-6.

12. Carrillo-Reid, L., Yang, W., Bando, Y., Peterka, D. S., & Yuste, R. (2016). Imprinting Cortical Ensembles. Science, 353(6300), 691–694. https://doi.org/10.1126/science.aaf7560

13. Costa, L. da F., Rodrigues, F. A., Travieso, G., & Boas, P. R. V. (2005). Characterization of complex networks: A survey of measurements. Advances in Physics, 56(1), 167–242. https://doi.org/10.1080/00018730601170527

14. Denk, W., Strickler, J. H., & Webb, W. W. (1990). Two-Photon Laser Scanning Fluorescence Microscopy. Science, 248(4951), 73–76.

15. Dong, W., Lee, R. H., Xu, H., Yang, S., Pratt, K. G., Cao, V., ... Aizenman, C. D. (2008). Visual Avoidance in Xenopus Tadpoles Is Correlated With the Maturation of Visual Responses in the Optic Tectum. Journal of Neurophysiology, 101(2), 803–815. https://doi.org/10.1152/jn.90848.2008

16. Eytan, D., & Marom, S. (2006). Dynamics and Effective Topology Underlying Synchronization in Networks of Cortical Neurons. Journal of Neuroscience, 26(33), 8465–8476. https://doi.org/10.1523/JNEUROSCI.1627-06.2006

17. Garofalo, M., Nieus, T., Massobrio, P., & Martinoia, S. (2009). Evaluation of the Performance of Information Theory- Based Methods and Cross-Correlation to Estimate the Functional Connectivity in Cortical Networks. PLoS ONE, 4(8). https://doi.org/10.1371/journal.pone.0006482

18. Grady, C. L., McIntosh, A. R., & Craik, F. I. M. (2003). Age-related differences in the functional connectivity of the hippocampus during memory encoding. Hippocampus, 13(5), 572–586. https://doi.org/10.1002/hipo.10114

19. Grynkiewicz, G., Poenie, M., and Tsien, R.Y. (1985). A new generation of Ca 2+ indicators with greatly improved fluorescence properties. J. Biol. Chem.260 , 3440–3450

20. Gurney, K. An Introduction to Neural Networks. London: Taylor & Francis, 2004.

21. Hamm, J. P., Peterka, D. S., Gogos, J. A., & Yuste, R. (2017). Altered Cortical Ensembles in Mouse Models of Schizophrenia. Neuron, 94(1), 153–167.e8 https://doi.org/10.1016/j.neuron.2017.03.019

22. Hastie T., Tibshirani R., Friedman J. (2009) Overview of Supervised Learning. In: The Elements of Statistical Learning. Springer Series in Statistics. Springer, New York, NY

23. Haydon, P. G. (2001). Glia : Listening and Talking To The Synapse. Nature Reviews Neuroscience, 2(March), 186–193.

24. Hecht-Nielsen, R. (1989). Theory of the Backpropagation Neural Network. Proceedings Of The International Joint Conference On Neural Networks, 1, 593–605. https://doi.org/10.1109/IJCNN.1989.118638

25. Hernández, J. M., & Mieghem, P. Van. (2011). Classification of graph metrics. Delft University of Technology.

26. Hodgkin, A. L., & Kats, B. (1949). The Effect of Sodium Ions on the Electrical Activity of the Giant Axon of the Squid. The Journal Of Physiology, 108(1), 37–77.

27. Hoffman, D. A., Magee, J. C., Colbert, C. M., & Johnston, D. (1997). K + channel regulation of signal propagation in dendrites of hippocampal pyramidal neurons. Nature, 387(June), 869–876.

28. Izhikevich, E. M. (2004). Which model to use for cortical spiking neurons? IEEE Transactions on Neural Networks. https://doi.org/10.1109/TNN.2004.832719

29. Katz, B., & Miledi, R. (1967). A Study of Synaptic Transmission in the Absence of Nerve Impulses. Department of Biophysics, University College London, 407–436.

30. Katz, B., & Miledi, R. (1968). The role of calcium in neuromuscular facilitation. Journal of Physiology, 195, 481–492. https://doi.org/10.1111/j.1365-3040.1992.tb01004.x

31. Khakhalin, A. S., Koren, D., Gu, J., Xu, H., & Aizenman, C. D. (2014). Excitation and inhibition in recurrent networks mediate collision avoidance in Xenopus tadpoles. European Journal of Neuroscience, 40(6), 2948–2962. https://doi.org/10.1111/ejn.12664

32. Knox, C. K. (1981). Detection of neuronal interactions using correlation analysis. Trends in Neurosciences, 4(C), 222–225. https://doi.org/10.1016/0166-2236(81)90070-9

33. Kunkel, Susanne, Morrison, Abigail, Weidel, Philipp, Eppler, Jochen Martin, Sinha, Ankur, Schenck, Wolfram, ... Plesser, Hans Ekkehard. (2017, March 1). NEST 2.12.0. Zenodo. http://doi.org/10.5281/zenodo.259534

34. Marblestone, A., Wayne, G., & Kording, K. (2016). Towards an integration of deep learning and neuroscience. https://doi.org/10.3389/fncom.2016.00094

35. Massobrio, P., Pasquale, V., & Martinoia, S. (2015). Self-organized criticality in cortical assemblies occurs in concurrent scale-free and small-world networks. Nature Publishing Group, (October 2014), 1–16. https://doi.org/10.1038/srep10578

36. McCulloch, W. S., & Pitts, W. H. (1943). A Logical Calculus of the Ideas Immanent In Nervous Activity. Bulletin of Mathematical Biophysics, 5, 115–133.

37. Miller, E. K., & Cohen, J. D. (2001). An Integrative Theory of Prefrontal Cortex Function. Annual Review of Neuroscience, 24, 167–202.

38. Minshew, N. J., & Williams, D. L. (2007). The New Neurobiology of Autism: Cortex, Connectivity, and Neuronal Organization. Archives of Neurology, 64(7), 945–950.

39. Mitchell, M. (1996). An Introduction to Genetic Algorithms (5th ed.). Cambridge, MA.: MIT Press.

40. Ntziachristos, V. (2010). Going deeper than microscopy : the optical imaging frontier in biology. Nature Publishing Group, 7(8), 603–614. https://doi.org/10.1038/nmeth.1483

41. Orrenius, S., Zhivotovsky, B., & Nicotera, P. (2003). Regulation of Cell Death: The Calcium - Apoptosis Link. Nature Review Molecular Cell Biology, 4(July), 552–565. https://doi.org/10.1038/nrm1150

42. Pajevic, S., & Plenz, D. (2009). Efficient network reconstruction from dynamical cascades identifies small-world topology of neuronal avalanches. PLoS Computational Biology, 5(1). https://doi.org/10.1371/journal.pcbi.1000271

43. Pandarinath, C., Shea, D. J., Collins, J., Jozefowicz, R., Stavisky, S. D., Kao, J. C., . . . Sussillo, D. (2017). Inferring single-trial neural population dynamics using sequential auto-encoders. bioRxiv.

   Retrieved from http://biorxiv.org/content/early/2017/06/20/152884.abstract

44. Paredes, R. M., Etzler, J. C., Watts, L. T., Zheng, W., & Lechleiter, J. D. (2008). Chemical calcium indicators. Methods, 46(3), 143–151. https://doi.org/10.1016/j.ymeth.2008.09.025

45. Porro, C. A., Francescato, M. P., Cettolo, V., Diamond, M. E., Baraldi, P., Zuiani, C., . . . Prampero, P. E. (1996). Primary Motor and Sensory Cortex Activation during Motor Performance and Motor Imagery : A Functional Magnetic Resonance Imaging Study. The Journal of Neuroscience, 16(23), 7688–7698.

46. Purves, D., Augustine, G. J., Fitzpatrick, D., Hall, W. C., LaMantia, A., and White, L. E. (2012). Neuroscience. Sunderland, Massachusetts.: Sinauer Associates, Inc.

47. Rakic, P. (2006). Evolution of the neocortex. Current Biology, 16(21), 910–914. https://doi.org/10.1038/nrn2719.Evolution

48. Robbins, H., & Monro, S. (1951). A Stochastic Approximation Method. The Annals of Mathematical Statistics, 22(3), 400–407.

49. Rubinov, M., & Sporns, O. (2010). Complex network measures of brain connectivity: Uses and interpretations. NeuroImage, 52, 1059–1069. https://doi.org/10.1016/j.neuroimage.2009.10.003

50. Ruder, S. (2016). An overview of gradient descent optimization algorithms. arXiv:1609.04747v2, 1–14.

51. Stetter O, Battaglia D, Soriano J, Geisel T (2012) Model-Free Reconstruction of Excitatory Neuronal Connectivity from Calcium Imaging Signals. PLo S Comput Biol 8(8): e1002653. doi:10.1371/journal.pcbi.1002653

52. Shimomura, O., Johnson, F. H. and Saiga, Y. (1962), Extraction, Purification and Properties of Aequorin, a Bioluminescent Protein from the Luminous Hydromedusan, Aequorea. J. Cell. Comp. Physiol., 59: 223–239. doi:10.1002/jcp.1030590302

53. Sporns, O., Chialvo, D., Kaiser, M., and Hilgetag, C. (2004). Organization, development and function of complex brain networks. Trends in Cognitive Sciences, 8(9), 418-425. doi:10.1016/j.tics.2004.07.008

54. Steels, L. (2007). Fifty Years of AI: From Symbols to Embodiment -and Back, 18–28.

55. Stetter, O., Battaglia, D., Soriano, J., and Geisel, T. (2012). Model-Free Reconstruction of Excitatory Neuronal Connectivity from Calcium Imaging Signals. PLoS Computational Biology. https://doi.org/10.1371/journal.pcbi.1002653

56. Strogatz, S. H. (2001). Exploring complex networks. Nature, 410(6825), 268–276. https://doi.org/10.1038/35065725

57. Svoboda, K., Yasuda, R., & Carolina, N. (2006). Principles of Two-Photon Excitation Microscopy and Its Applications to Neuroscience. Neuron, 50, 823–839. https://doi.org/10.1016/j.neuron.2006.05.019

58. Terry, R. D., Masliah, E., Salmon, D. P., Butters, N., Deteresa, R., Hill, R., . . . Katzman, R. (1991). Physical Basis of Cognitive Alterations in Alzheimer ' s Disease : Synapse h s s Is the Major Correlate of Cognitive Impairment. Annals of Neurology, 30(4), 572–580.

59. Tetzlaff, C., Okujeni, S., Egert, U., Wörgötter, F., & Butz, M. (2010). Self-organized criticality in developing neuronal networks. PLoS Computational Biology, 6(12). https://doi.org/10.1371/journal.pcbi.1001013

60. Turing, A. M. (2009). Computing machinery and intelligence. In Parsing the Turing Test: Philosophical and Methodological Issues in the Quest for the Thinking Computer. https://doi.org/10.1007/978-1-4020-6710-5_3

61. Werbos, P. J. (1990). Backpropagation Through Time: What It Does and How to Do It. Proceedings of the IEEE, 78(10), 1550–1560. https://doi.org/10.1109/5.58337

62. Widrow, B., & Lehr, M. A. (1990). 30 Years of Adaptive Neural Networks: Perceptron, Madaline, and Backpropagation. Proceedings of the IEEE, 78(9), 1415–1442. https://doi.org/10.1109/5.58323

63. Xu, H., Khakhalin, A. S., Nurmikko, A. V., & Aizenman, C. D. (2011). Visual Experience-Dependent Maturation of Correlated Neuronal Activity Patterns in a Developing Visual System. Journal of Neuroscience, 31(22), 8025–8036. https://doi.org/10.1523/JNEUROSCI.5802-10.2011

64. Zhou, D., Xiao, Y., Zhang, Y., Xu, Z., & Cai, D. (2014). Granger causality network reconstruction of conductance-based integrate-and-fire neuronal systems. PLoS ONE, 9(2). https://doi.org/10.1371/journal.pone.0087636

65. Zucker, R. S. (1999). Calcium- and activity-dependent synaptic. Current Opinion in Neurobiology, 9(3), 305–313.